Multimodal and multiplex spectral imaging of rat cornea ex vivo using a white-light laser source

Hiroki Segawa, Yuichi Kaji, Philippe Leproux, Vincent Couderc, Takeaki Ozawa, Tetsuro Oshika, Hideaki Kano

J. Biophotonics **8**, No. 9, 705–713 (2015) / **DOI** 10.1002/jbio.201400059

Journal of BIOPHOTONICS

FULL ARTICLE

Multimodal and multiplex spectral imaging of rat cornea *ex vivo* using a white-light laser source

Hiroki Segawa[1], *Yuichi Kaji*[2], *Philippe Leproux*[3], *Vincent Couderc*[3], *Takeaki Ozawa*[1], *Tetsuro Oshika*[2], *and Hideaki Kano*[*, 4]

[1] Department of Chemistry, School of Science, The University of Tokyo, 7-3-1, Hongo, Bunkyo, Tokyo, 113-0033, Japan
[2] Graduate School of Comprehensive Human Science, University of Tsukuba, 1-1-1 Tennodai, Tsukuba, Ibaraki, 305-8575, Japan
[3] Xlim Research Institute, CNRS-University of Limoges, 123 Avenue Albert Thomas, 87060 Limoges cedex, France
[4] Institute of Applied Physics, University of Tsukuba, 1-1-1 Tennodai, Tsukuba, Ibaraki, 305-8573, Japan

Received 30 May 2014, revised 24 July 2014; 8 September 2014, accepted 13 October 2014
Published online 7 November 2014

Key words: spectrum analysis Raman/instrumentation, molecular imaging, multimodal imaging, cornea

We applied our multimodal nonlinear spectral imaging microscope to the measurement of rat cornea. We successfully obtained multiple nonlinear signals of coherent anti-Stokes Raman scattering (CARS), third-order sum frequency generation (TSFG), and second harmonic generation (SHG). Depending on the nonlinear optical processes, the cornea tissue was visualized with different image contrast mechanism simultaneously. Due to white-light laser excitation, multiplex CARS and TSFG spectra were obtained. Combined multimodal and spectral analysis clearly elucidated the layered structure of rat cornea with molecular structural information. This study indicates that our multimodal nonlinear spectral microscope is a promising bioimaging method for tissue study.

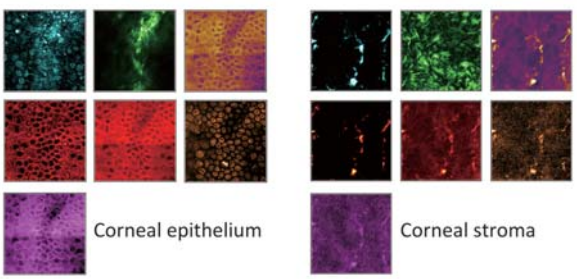

Multimodal nonlinear spectral images of rat cornea at corneal epithelium and corneal stroma in the in-plane (XY) direction. With use of the combinational analysis of different nonlinear optical processes, detailed molecular structural information is available without staining or labelling.

1. Introduction

In vivo and *in situ* visualization of biological tissue components without staining and molecular tagging are of considerable importance in biological and medical science. Optical coherence tomography [1] or confocal microscopy [2] are widely used for *in situ* imaging of the biological tissue. Both two techniques are capable of capturing micrometer-resolution, three-dimensional images from optical scattering media. However, they provide limited image contrast and poor molecular specificity due to their contrast mechanisms, which rely on spatial variations of refractive indices.

Recently, multiphoton microscopy has attracted much attention. Multiphoton microscopy is based on the nonlinear interactions between molecules and photons. Two or three photons from a pulsed near-infrared (NIR) laser source are focused onto a sample to generate one photon in the spectral range different from those of the input photons. The signal is generated from a tightly-focused confined volume, resulting in three-dimensional sectioning capability. So far, various kinds of nonlinear optical processes

* Corresponding author: e-mail: hkano@bk.tsukuba.ac.jp, Phone: +81 29 853 5421

such as two- or three-photon excited fluorescence [3, 4], second- or third-harmonic generation (SHG or THG) [5–11], sum frequency generation (SFG) [12], third-order sum frequency generation (TSFG) [13], coherent anti-Stokes Raman scattering (CARS) [14–16] and stimulated Raman scattering (SRS) [17–19] have been applied to microscopy. Since these nonlinear optical processes simultaneously take place, we are able to combine various multiphoton microscopic techniques [13, 20]. This multimodality offers exclusive capabilities to obtain information on molecular composition, organization, and dynamics in an unstained or unlabeled tissue, which is not accessible using other noninvasive methods.

By using a spectrometer, spectral imaging can be performed using a single excitation laser source. In order to extend the spectral coverage of the excitation laser, a supercontinuum (SC) white-light source is applicable. The SC, or white-light laser source, can be generated by seeding laser pulses into a photonic crystal fiber (PCF) [21]. The temporal duration of SC are ranging from femtosecond to nanosecond, depends on that of the seeding laser. In our previous study, we have developed tetra-modal (CARS, SHG, THG and TSFG) and multiplex microspectroscopy using sub-nanosecond NIR excitation (1064–1600 nm), and applied it to imaging of living yeast cells [13]. The NIR excitation is also advantageous in particular to imaging of the tissue sample due to suppression of photodamage and large penetration depth.

In the present study, we evaluated the applicability of our multimodal multiphoton spectral microscope to imaging of biological tissues, in particular for rat cornea *ex vivo*. Cornea is transparent tissue, which is positioned at the front part of eye. It functions as an external wall of eye and lens, and plays an important role in vision. The rat cornea is known to have a layered structure. Concerning the rat cornea, it consists of corneal epithelium, Bowman's layer, corneal stroma, Descemet's membrane, and corneal endothelium. Although cornea is transparent, previous studies of multiphoton microscopy revealed the inner structure of cornea without staining by the use of SHG and THG [22, 23]. CARS and two-photon auto-fluorescence (TPAF) were also applied to visualizing mouse cornea, and distributions of lipid and protein have been reported [24]. On the other hand, typical diagnostic method such as the slit-lamp examination cannot allow us to investigate the layered structure of transparent cornea. Many cornea diseases such as diabetic keratopathy, however, is known to be developed even when cornea is transparent. The molecular-level diagnostic method which reveals molecular structure of transparent cornea, and identify the types and the location of the disease, is thus crucial for next-generation eye diagnosis. However, previous CARS study is focused only on the CH stretch vibrational modes, which provide poor and indirect information on molecular structure and conformation. Our multimodal and multiphoton imaging technique is capable of multiplex CARS spectral imaging in the molecular fingerprint region (800–1800 cm^{-1}) as well as the CH stretch region. Therefore our spectral imaging method possibly becomes one of the promising diagnostic tools.

2. Experimental

2.1 Multimodal and multiplex spectral imaging system

The schematic diagram of our setup is shown in Figure 1. The detail is described elsewhere [13, 25]. Briefly, the light source is a cw Q-switched microchip Nd : YAG laser. The temporal duration, output power, and repetition rate are 800 ps, 300 mW, and 33 kHz, respectively. The output beam is divided into two. The one is used directly (1064 nm) as the pump radiation (ω_1). The other is used as seed laser pulses which are introduced into a PCF to generate SC (white-light laser) for Stokes radiation (ω_2). With using a long-pass filter, only the NIR spectral component (>1064 nm) is extracted. Two radiations are superimposed by a notch filter, and are tightly focused by the microscope objective (Nikon CFI Plan Apo 60×/NA 1.2) in a custom-made microscope. The laser power at the sample point was 20 mW (ω_1) and 15 mW (ω_2), respectively. The transmitted

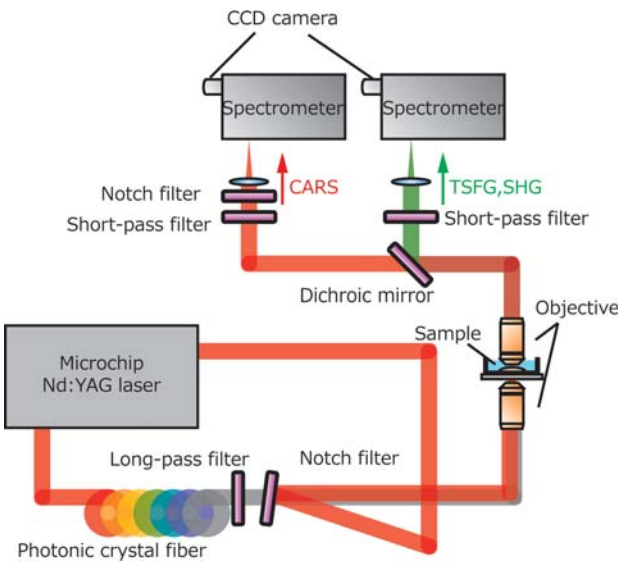

Figure 1 Schematic diagram of the setup of multimodal (TSFG, SHG and CARS) and multiplex spectral imaging system.

TSFG, SHG and CARS signals are collected by a water-dip microscope objective (Nikon Apo NIR 60×/NA 1.0). With use of a visible/NIR dichroic mirror, CARS in NIR, and TSFG and SHG in UV-visible are spectrally separated, and are detected by two spectrometers. The sample is mounted on a three-dimensional piezo electric stage (PZT), and the signal is acquired by raster scanning. The exposure time is 100 msec/pixel. The pixel size is 500 nm in the in-plane (XY) direction and 1 μm in the depth (Z) direction.

2.2 Sample preparation

12- to 16-week-old male Long Evans rats, each weighing 250 g to 400 g (Charles River Laboratories), were used. All animals were treated in accordance with the ARVO Statement for the Use of Animals in Ophthalmic and Vision Research. Experimental protocols were approved from the animal ethics review board in University of Tsukuba. Each rat was anesthetized by intraperitoneal injection of pentobarbital (25 mg/kg of body weight). Under an operating microscope, corneas of the eyes were excised. The corneas were soaked in normal saline, and then placed between a glass bottom dish and a cover glass.

3. Results and discussion

Figure 2 shows spectral profiles of the signals due to multiple nonlinear optical processes in the UV-visible-NIR regions at four different corneal positions (red and blue: corneal epithelium, green: interface between corneal epithelium and stroma, yellow: corneal stroma). Owing to the combined excitation with the SC and 1064 nm laser pulses, multiple nonlinear optical processes simultaneously take place in the UV-visible-NIR regions. Hereafter, we assign the signals in different spectral domain to each nonlinear optical process. The signal around 380 nm with a broad spectral profile is assigned to multiplex TSFG mainly due to $2\omega_1 + \omega_2$. It has been reported previously by our group [13], and the spectral profile is

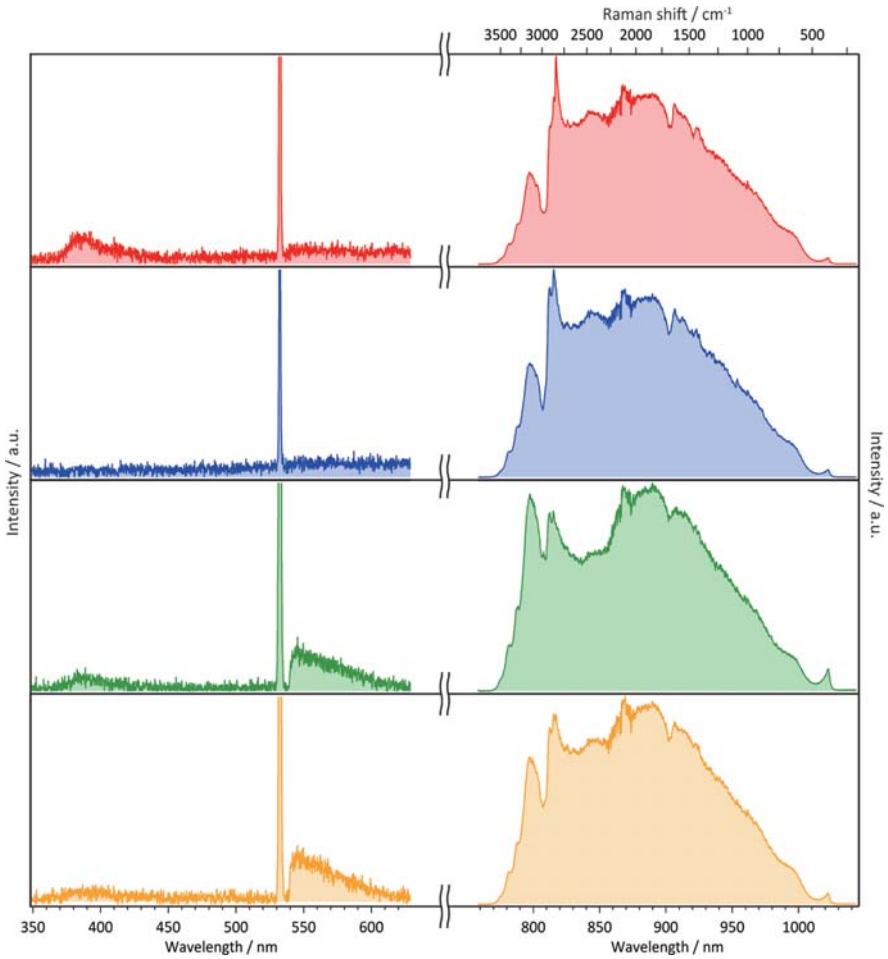

Figure 2 Spectral profiles of the nonlinear optical signals in the visible and NIR regions at four different corneal positions (red and blue: corneal epithelium, green: interface between epithelium and stroma, yellow: corneal stroma).

similar to the previous report. In the present study, it was hard to observe the THG signal at 355 nm ($3\omega_1$). This is because of the water-dip microscope objective for the signal collection, which has low transmittance in the UV region. There are other two signals in visible wavelength region. The signal at 532 nm with a sharp spectral profile is assigned to SHG ($2\omega_1$). According to previous studies [5–11, 22], strong SHG signal is obtained from collagen fibers. As described later, the SHG signal reflects the orientation and distribution of the collagen fibers. The signal around 550 nm with a broad spectral profile is assigned to multiplex SFG due to $\omega_1 + \omega_2$, which in general provides similar information to that of SHG. In NIR region, sharp and dispersive spectral profiles are superimposed on the broad background. They are typical spectral profiles of the multiplex CARS spectra. The origin of broad background is so-called nonresonant background (NB) [25]. Although NB should provide a flat spectral profile, the raw spectral profile is distorted mainly due to spectral profile of the SC and wavelength-dependent sensitivity of the spectrometer. The dispersive lineshapes are caused by the interference of the vibrationally resonant CARS signals with the NB [25]. As shown in the upper axis in Figure 2, almost all fundamental Raman bands are simultaneously observed by using the white-light Stokes pulses.

Figure 3 shows the spectral profiles of the imaginary part of the CARS signal (Im $[\chi^{(3)}]$), each of which is retrieved from the spectra shown in Figure 2. These Im $[\chi^{(3)}]$ spectra were calculated by maximum entropy method (MEM) [25]. The MEM does not require any *a priori* knowledge of the vibrational bands but still is able to retrieve the phase information on the third-order nonlinear susceptibility $\chi^{(3)}$, whose imaginary part corresponds to ordinary (spontaneous) Raman spectra [26]. Therefore, the intensity of the retrieved band, Im $[\chi^{(3)}]$, is proportional to the molecular concentration. In other words, each band can be evaluated quantitatively. The capability of quantitative spectral analysis attained by the combination of multiplex CARS and MEM is one of the most important advantages of our system. It is noted that we have performed noise filtering of the Im $[\chi^{(3)}]$ spectra by using the singular value decomposition (SVD) analysis [27]. The Im $[\chi^{(3)}]$ spectra show rich information on the molecular composition of the cornea tissue. The strong band around 2900 cm^{-1} is assigned as the CH stretch vibrational modes. This broad band is the superposition of the CH_3 stretch vibrational mode (2932 cm^{-1} and 2871 cm^{-1}) and CH_2 stretch vibrational mode (2847 cm^{-1}). CH_3 stretch mode is widely used as the marker band of protein molecules. On the other hand, CH_2 stretch band is used for probing the distribution of lipid molecules [14]. Compared with blue, green and yellow spectra, red spectrum shows

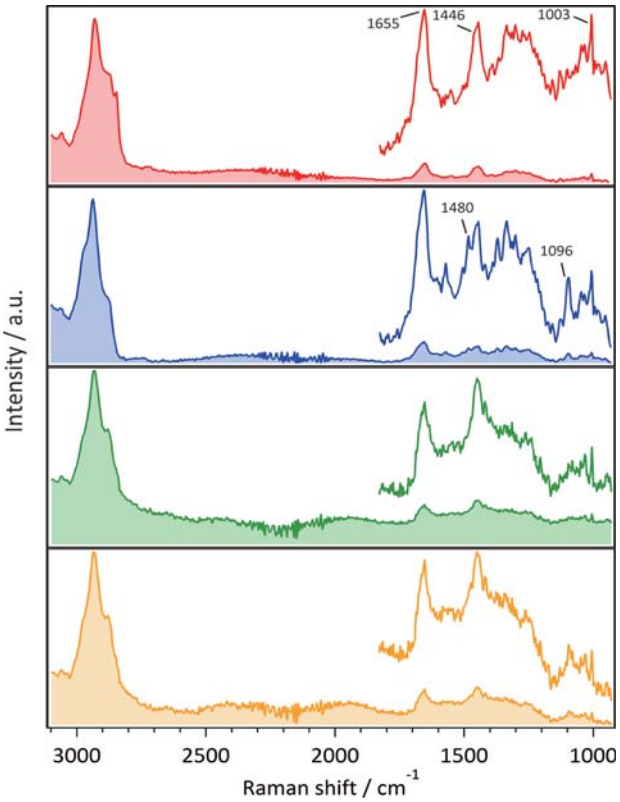

Figure 3 Spectral profiles of the imaginary part of the CARS signal (Im $[\chi^{(3)}]$) calculated by maximum entropy method at four different corneal positions (red and blue: corneal epithelium, green: interface between epithelium and stroma, yellow: corneal stroma). Inset in each image is enlarged fingerprint region spectrum.

relatively strong intensity of CH_2 stretch mode. This means that the concentration of lipid molecules at red position is higher than those at another positions (blue, green and yellow). In the fingerprint region (800–1800 cm^{-1}) shown in inset of Figure 3, there are many bands correspond to various skeletal vibration modes, which are highly sensitive to the molecular structure (molecular fingerprint). Although almost all bands are weak, our multiplex CARS technique with MEM and SVD analysis clearly reveals each vibrational mode. The band at 1655 cm^{-1} is assigned as the superposition of the *cis* C=C stretch of lipid chains and the amide I mode of proteins. The band at 1446 cm^{-1} is assigned to the CH bend mode, in which two CH bend modes, namely CH_2 scissors and CH_3 degenerate deformation, are overlapped [25]. The sharp band at 1003 cm^{-1} is assigned to the phenylalanine residues in proteins. Besides the above mentioned bands, we can find several site-specific Raman bands. For example, the band at 1480 cm^{-1}, clearly shown in the blue spectrum, is assigned as the purine ring stretch mode [28]. This mode can be used as a marker band for purine bases such as adenine and guanine. This band is recogniz-

able also in the yellow spectrum at the shoulder of the strong 1446 cm^{-1} band. In the blue spectrum, we can recognize the strong 1096 cm^{-1} band, corresponding to PO_2^- stretch of phosphate group. This band is used as the marker band of nucleic acid. In the yellow spectrum, we can recognize weak 1096 cm^{-1} band. The capability of such detailed spectral investigation and discrimination is one of the most significant advantages of our spectral imaging method.

Multimodal and multiplex images are reconstructed by calculating the signal intensity of each spectral band in Figure 3 through curve fitting using the sum of Gaussian functions. Figure 4(a–g) are constructed images of rat cornea in the depth (XZ) direction. Each image corresponds to (a) TSFG, (b) SHG, (c) CARS at CH_3 stretch (protein, lipid), (d) CARS at CH_2 stretch (lipid), (e) CARS at CH bend (protein, lipid), (f) CARS at purine-ring stretch (purine base), and (g) CARS at phenylalanine residues (protein), respectively. We also show a typical Hematoxylin and Eosin (H&E) stained histological image (Figure 4(h)) as a reference which was prepared from the frozen section of a cornea tissue sample different from Figure 4(a–g). To the best of our knowledge, this is the first report on the *ex vivo* multimodal tissue imaging with the use of the fingerprint CARS spectrum. The scanning area of these images is 25 μm in the in-plane direction and 175 μm in the depth direction. Due to the NIR excitation, deeply penetrated images of cornea are successfully obtained. The acquisition time of these images is about 15 min. It should be noted that the limitation of the depth scanning is determined by maximum stroke of the PZT stage rather than the scattering of the excitation radiations. Depending on the nonlinear optical processes and vibrational resonances, we are able to obtain various images with different information simultaneously. In Figure 4(a–g), two layers are visualized, namely corneal epithelium and corneal stroma (see Figure 4(h)). The upper and lower regions in Figure 4(a–g) correspond to corneal epithelium and corneal stroma, respectively. In corneal epithelium, strong CARS signals are observed (Figure 4(c–g)). This structure is assigned as epithelial cells because all lipid, protein and purine base CARS signals are obtained. As discussed in detail later, TSFG signals are also obtained from some epithelial cells (Figure 4(a)). In corneal stroma, SHG image (Figure 4(b)) visualizes the structure different from that observed by the other images. This SHG image indicates the distribution of collagen fibers because corneal stroma contains a lot of collagen fibrils, which generate strong SHG signals [5–11, 22]. TSFG and CARS images (Figure 4(a) and (c–g)) visualize the flat structures. Similar to epithelial cells, all lipid, protein and purine base CARS signals are obtained from these flat structures. The size and distribution of this flat structure are quite similar to keratocytes observed in the H&E stained image (Figure 4(h)) in stroma. We thus assign these structures to keratocytes. Keratocyte is one type of fibroblasts, which is activated only when the cornea is damaged. Due to the flat structure, interface-sensitive TSFG signals are observed at keratocytes. At the interface of corneal epithelium and stroma, a thin membrane-like structure is clearly observed in Figure 4(a). Interestingly, this structure is not highlighted in the other images (Figure 4(b–g)). Taking into consideration the contrast mechanism of TSFG, optical heterogeneity should exist at this area. Based on the result that the TSFG image at this area gives uniform intensity distribution, it is reasonable to assume the existence of a layered structure between epithelium and stroma. From the histological point of view, this structure is assignable to epithelial basement membrane or Bowman's layer. The main molecular components of basement membrane are nonfibrous type-IV collagens, and those of Bowman's layer are fibrous type-I collagens. Due to this higher order structural difference of collagens, SHG signals generate only from type-I, and not from type-IV

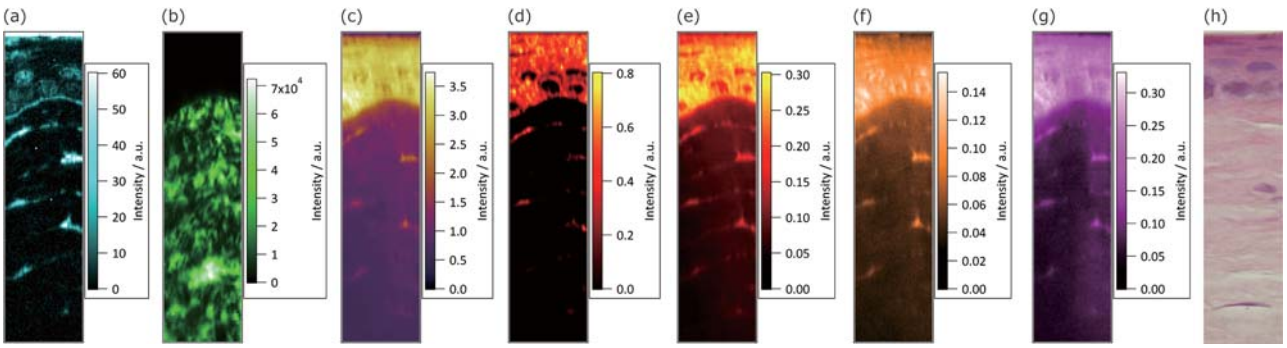

Figure 4 Multimodal and multiplex spectral imaging of the rat cornea tissue in the depth (XZ) direction; (**a**) TSFG, (**b**) SHG, (**c**) CARS at CH_3 stretch, (**d**) CARS at CH_2 stretch, (**e**) CARS at CH bend, (**f**) CARS at purine-ring stretch, (**g**) CARS at phenylalanine residues, (**h**) referential H&E stained image of frozen section of rat cornea different from (**a–g**). The top part corresponds to the corneal epithelium. The image corresponds to 25 × 175 μm^2.

[29]. Therefore, SHG signal should be obtained only from the Bowman's layer, not from basement membrane. In our SHG image, however, it is difficult to observe SHG signal between epithelium and stroma. This is partly because of the thin thickness of rat corneal Bowman's layer (about 1 μm). Basement membrane is thinner than Bowman's layer, and adhere to Bowman's layer. Taking account of present spatial resolution in the depth direction of our setup (about 4 μm), it is difficult to clearly differentiate basement membrane and Bowman's layer. At present, we thus assign this structure as the complex of basement membrane and Bowman's layer. Finally, the top edge of Figure 4(a) corresponds to the interface of the cornea tissue and cover glass.

In order to investigate corneal structures in more detail, we measured in-plane (XY) images of rat cornea. Figures 5(a–g) and 6(a–g) show the results of multimodal and multiplex spectral imaging in the in-plane direction. Each figure corresponds to the depth positions at corneal epithelium (Figure 5) and stroma (Figure 6), respectively. The scanning area is 100×100 μm^2. Since the spatial resolution in the in-plane direction is better than that in the depth direction, detailed structures inside each layer are clearly visualized. First, CARS at CH_2 stretch vibrational mode (lipid) image (Figure 5(d)) shows a honeycomb-like structure assigned as cell membrane. It should be noted that cell membrane in general does not provide a strong CARS signal at CH_2 stretch in the case of single mammalian cells. The highlighted cell-membrane image obtained in the present study should be the characteristic of epithelial cells in tissue sample possibly due to the closely packing of each cell. Focusing on phenylalanine residue CARS image (protein, Figure 5(g)), we can also recognize the honeycomb-like structure. In this image, moderate intensity of the CARS signal is observed from cytoplasm. CH_3 stretch and CH bend CARS images (Figure 5(c), (e)) are similar to the superposition of lipid (Figure 5(d)) and protein (Figure 5(g)) images. This means that cellular membrane in corneal epithelium are lipid and protein rich in order to construct closely packed structures. On the other hand, the signal distribution of CARS at purine-ring vibrational mode (Figure 5(f)) is totally different from above the other CARS images. In this image the cell membrane is not highlighted and the strong signal is observed at the center part of epithelial cells. Taking into account that the purine base is one of the major components of DNA, nuclei of epithelial cells should be highlighted in Figure 5(f). The distribution of the molecules with the purine ring is inhomogeneous, and some cells show the doughnut-shaped structures. These structures possibly reflect the intranuclear distribution of DNA, RNA or nucleotide molecules such as ATP, all of which possess purine ring and are detectable by CARS at the purine-ring vibrational mode.

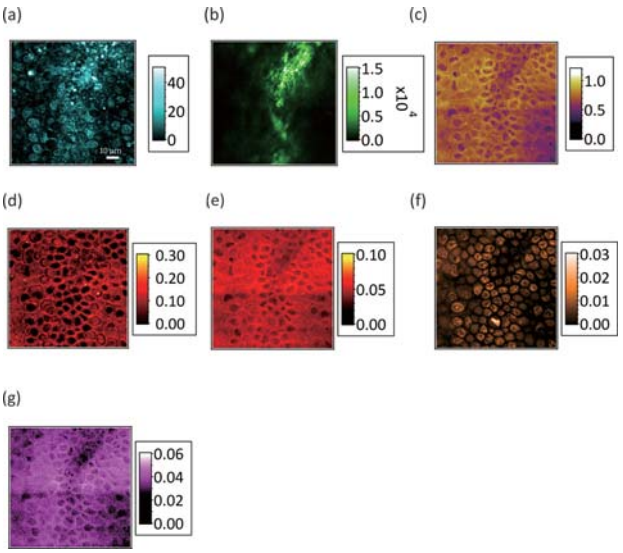

Figure 5 Multimodal and multiplex spectral imaging of corneal epithelium in the in-plane (XY) direction; (**a**) TSFG, (**b**) SHG, (**c**) CARS at CH_3 stretch, (**d**) CARS at CH_2 stretch, (**e**) CARS at CH bend, (**f**) CARS at purine-ring stretch, (**g**) CARS at phenylalanine residues. The image corresponds to 100×100 μm^2.

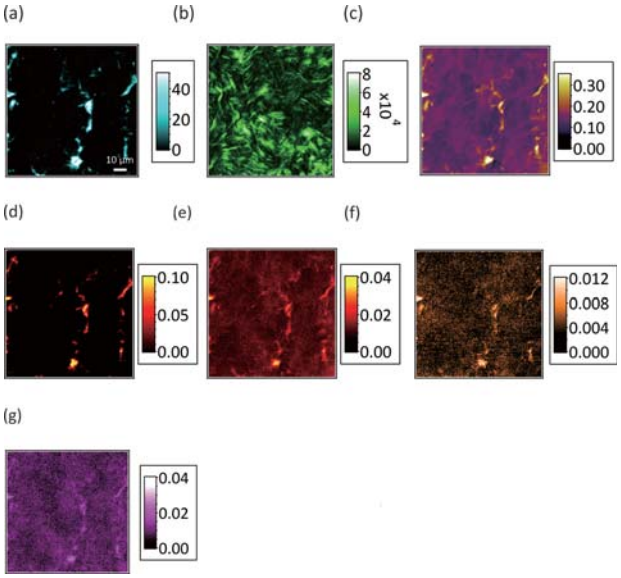

Figure 6 Multimodal and multiplex spectral imaging of corneal stroma in the in-plane (XY) direction; (**a**) TSFG, (**b**) SHG, (**c**) CARS at CH_3 stretch, (**d**) CARS at CH_2 stretch, (**e**) CARS at CH bend, (**f**) CARS at purine-ring stretch, and (**g**) CARS at phenylalanine residues. The image corresponds to 100×100 μm^2.

Compared with the CARS purine-ring image (Figure 5(f)), TSFG image (Figure 5(a)) also shows intracellular structures. Since the contrast mechanism of TSFG is inhomogeneity of refractive index or nonlinear optical susceptibility, Figure 5(a) means

that the inside of each epithelial cell is inhomogeneous. In Figure 5(a), a speckle-like pattern is found. This pattern is not visualized in all the other images (Figure 5(b–g)). On the other hand, SHG image (Figure 5(b)) shows clear contrast only around the upper-center part, where TSFG spot-like patterns are observed. Since the image is obtained near the boundary between corneal epithelium and stroma, or Figure 5(b) is similar to Figure 4(b), we consider that stroma intrudes into the same depth position of epithelium layer.

In corneal stroma, images are totally different from those obtained in corneal epithelium. As mentioned in the depth direction images, flat keratocytes are sparsely observed in Figures 6(a) and 6(c–g). The main component of corneal stroma is type-I collagen fibers, which are clearly observed with ordered arrangement in the SHG image (Figure 6(b)). Since SHG is sensitive to the filamentous structure, it is reasonable that SHG signal from type-I collagen in stroma is clearly observed.

Lastly we performed three-dimensional (XYZ) multimodal multiplex spectral images of rat cornea *ex vivo*. Totally 21 lateral (XY) images (40×40 μm^2) are obtained with each 7.5 μm depth difference. The total acquisition time is about 3.9 hours. Figure 7 show some of 21-depth resolved images, namely, 5 images with equidistant 22.5 μm depth positions from corneal epithelium (top) to stroma (bottom). The full movies of the image acquisition are available in supporting information (Figure S(a–g)). Since the optical axis of cornea tissue depends on the position of the sample, the laboratory coordinate (XYZ) is different from the optical axis of cornea. In Figure 7, the left below part of the tissue is closer to the cover glass than the upper right. From the position of corneal epithelium to that of stroma, TSFG, SHG, and multiplex CARS images show characteristic depth dependence on their nonlinear optical responses and their chemical specificities. In particular, doughnut-like and spot-like patterns are observed at the center and the edge of corneal epithelium (See Figure S(a)). These patterns probably detect the boundary of nuclei in three-dimensional view.

4. Conclusion

In the present study, we applied multimodal and multiplex spectral imaging with CARS, SHG and TSFG to *ex vivo* imaging of rat cornea. To the best of our knowledge, this is the first report on the *ex vivo* multimodal tissue imaging with the use of the fingerprint CARS spectrum. Depending on the nonlinear optical properties, cornea sample is visualized with different image contrast. TSFG visualizes intracellular structure in corneal epithelium. TSFG also gives clear contrast to the membrane-like structure between corneal epithelium and corneal stroma. This structure is assigned as the complex of basement membrane and Bowman's layer. Recently we

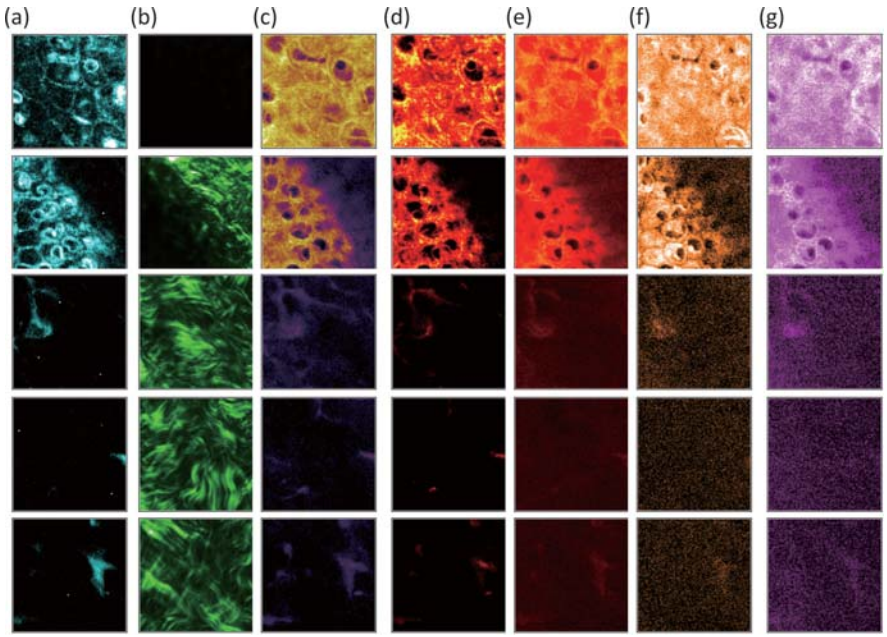

Figure 7 Multimodal and multiplex spectral imaging of the rat cornea tissue in the three-dimensional (XYZ) direction; (**a**) TSFG (S(a)), (**b**) SHG (S(b)), (**c**) CARS at CH_3 stretch (S(c)), (**d**) CARS at CH_2 stretch (S(d)), (**e**) CARS at CH bend (S(e)), (**f**) CARS at purine-ring stretch (S(f)), and (**g**) CARS at phenylalanine residues (S(g)). The image corresponds to 40×40 μm^2.

have developed electronically resonant multiplex TSFG spectroscopy [30]. It will thus be able to analyze electronic state of biomolecules inside cornea or other tissues *ex vivo*. On the other hand, SHG clearly visualizes type-I collagen fibrils in corneal stroma. It is also important in diagnostics. Disorder of the arrangement of type-I collagen fiber induces severe effects on vision. SHG intensity and polarization dependence can be used to visualize the arrangement of type-I collagen fibers, and to discriminate type-I (SHG active) from type-IV (SHG inactive) collagens [29]. When corneal stroma is damaged, keratocytes are activated. Subsequently, they produce type-IV collagens in order to infill the damaged area. Based on the SHG intensity and polarization dependence, we can monitor the wound healing process through rearrangement and distribution of type-I collagens. This quaternary structure difference of collagens is possibly distinguished by CARS spectra. It is thus expected that we will be able to quantitatively evaluate the healing process using Im $[\chi^{(3)}]$ spectra, which gives quantitative information, or the intensity of which is proportional to the number of molecules in the focal volume. The multiplex CARS technique provides molecular specific vibrational images. The purine ring signal visualizes cell nuclei and intranuclear DNA distribution. Thanks to the NIR excitation, photodamage is expected to be lowered and deeply penetrated images are obtained. This study proves that multimodal and mutilpex microspectroscopy provides valuable information on the microscopic properties of the cornea *ex vivo* and *in vivo* in the near future. Although the present long image-acquisition time is insufficient to apply our present system to clinical use, further improvement of the experiment setup, including the modification to the back-scattering configuration (epi detection), possibly supports pathologists as a powerful label-free imaging tool. This technique provides huge potential for mini- or non-invasive, real-time cornea and other tissue study or diagnostics.

Supporting Information

Additional supporting information may be found in the online version of this article at the publisher's website.

Acknowledgements This work is supported by JSPS bilateral joint research project (SAKURA program) and The NOVARTIS Foundation (Japan) for the Promotion of Science. The authors thank the LEUKOS company for technical support with the dual-output supercontinuum light source. The authors gratefully acknowledge J. Ukon, UKON CRAFT SCIENCE, Ltd. for assisting with a fruitful collaboration between Japanese and French labs.

Author biographies Please see Supporting Information online.

References

[1] W. Drexler and J. G. Fujimoto, Prog. Retin. Eye Res. **27**, 45–88 (2008).
[2] R. F. Guthoff, A. Zhivov, and O. Stachs, Clin. Experiment. Ophthalmol. **37**, 100–117 (2009).
[3] R. Sharma, L. Yin, W. H. Merigan, G. Palczewska, K. Palczewski, D. R. Williams, and J. J. Hunter, Biomed. Opt. Express **4**, 1285–1293 (2013).
[4] N. Horton, K. Wang, D. Kobat, and C. Clark, Nat. Photonics **7**, 205–209 (2013).
[5] M. Savoldelli, M. Merano, D. Donate, O. Albert, V. Nuzzo, G. Mourou, J.-M. Legeais, K. Plamann, and P. F. G. Rodríguez, J. Biomed. Opt. **12**, 064032–064032-11 (2007).
[6] S.-Y. Chen, H.-C. Yu, C.-K. Sun, and I.-J. Wang, J. Biomed. Opt. **14**, 044012–044012-7 (2009).
[7] S. W. Teng, H. Y. Tan, J. L. Peng, H. H. Lin, K. H. Kim, W. Lo, Y. Sun, W. C. Lin, S. J. Lin, S. H. Jee, P. T. C. So, and C. Y. Dong, Invest. Ophthalmol. Vis. Sci. **47**, 1216–1224 (2006).
[8] J. M. Bueno, E. J. Gualda, A. Giakoumaki, P. Pérez-Merino, S. Marcos, and P. Artal, Invest. Ophthalmol. Vis. Sci. **52**, 5325–5331 (2011).
[9] M. Han, G. Giese, and J. F. Bille, Opt. Express **13**, 5791–5797 (2005).
[10] A. T. Yeh, N. Nassif, A. Zoumi, and B. J. Tromberg, Opt. Lett. **27**, 2082–2084 (2002).
[11] P. Steven, M. Hovakimyan, R. F. Guthoff, G. Hüttmann, and O. Stachs, J. Cataract Refract. Surg. **36**, 2150–2159 (2010).
[12] V. Raghunathan, Y. Han, O. Korth, N.-H. Ge, and E. O. Potma, Opt. Lett. **36**, 3891–3893 (2011).
[13] H. Segawa, M. Okuno, H. Kano, P. Leproux, V. Couderc, and H. O. Hamaguchi, Opt. Express **20**, 9551–9557 (2012).
[14] J. P. Pezacki, J. A. Blake, D. C. Danielson, D. C. Kennedy, R. K. Lyn, and R. Singaravelu, Nat. Chem. Biol. **7**, 137–145 (2011).
[15] C.-Y. Chung, J. Boik, and E. O. Potma, Annu. Rev. Phys. Chem. **64**, 77–99 (2013).
[16] C. L. Evans and X. S. Xie, Annu. Rev. Anal. Chem. **1**, 883–909 (2008).
[17] C. W. Freudiger, W. Min, B. G. Saar, S. Lu, G. R. Holtom, C. He, J. C. Tsai, J. X. Kang, and X. S. Xie, Science **322**, 1857–1861 (2008).
[18] Y. Ozeki, W. Umemura, and Y. Otsuka, Nat. Photonics **6**, 845–851 (2012).
[19] M. C. Wang, W. Min, C. W. Freudiger, G. Ruvkun, and X. S. Xie, Nat. Methods **8**, 135–138 (2011).
[20] S. H. Parekh, Y. J. Lee, K. A. Aamer, and M. T. Cicerone, Biophys. J. **99**, 2695–2704 (2010).
[21] J. K. Ranka, R. S. Windeler, and A. J. Stentz, Opt. Lett. **25**, 25–27 (2000).

[22] F. Aptel, N. Olivier, A. Deniset-Besseau, J.-M. Legeais, K. Plamann, M.-C. Scbanne-Klein, and E. Beaurepaire, Investig. Ophthalmol. Vis. Sci. **51**, 2459–2465 (2010).
[23] N. Olivier, F. Aptel, K. Plamann, M.-C. Schanne-Klein, and E. Beaurepaire, Opt. Express **18**, 5028–5040 (2010).
[24] D. A. Ammar, T. C. Lei, M. Y. Kahook, and O. Masihzadeh, Invest. Ophthalmol. Vis. Sci. **54**, 5258–5265 (2013).
[25] M. Okuno, H. Kano, P. Leproux, V. Couderc, J. P. R. Day, M. Bonn, and H. Hamaguchi, Angew. Chem. Int. Ed. **49**, 6773–6777 (2010).
[26] E. M. Vartiainen, H. A. Rinia, M. Müller, and M. Bonn, Opt. Express **14**, 3622–3630 (2006).
[27] H.-J. van Manen, Y. M. Kraan, D. Roos, and C. Otto, J. Phys. Chem. B **108**, 18762–18771 (2004).
[28] A. Toyama, N. Hanada, J. Ono, E. Yoshimitsu, and H. Takeuchi, J. Raman Spectrosc. **30**, 623–630 (1999).
[29] A.-M. Pena, T. Boulesteix, T. Dartigalongue, and M.-C. Schanne-Klein, J. Am. Chem. Soc. **127**, 10314–10322 (2005).
[30] H. Segawa, N. Fukutake, P. Leproux, V. Couderc, T. Ozawa, and H. Kano, Opt. Express **22**, 10416–10429 (2014).